SIAM J. APPL. MATH.
Vol. 56, No. 1, pp. 119–142, February 1996

007

A DELAY EQUATION REPRESENTATION OF PULSE CIRCULATION ON A RING IN EXCITABLE MEDIA*

MARC COURTEMANCHE†, JAMES P. KEENER‡, AND LEON GLASS§

Abstract. This paper develops a theory for pulse circulation on a ring in a continuous excitable medium. Simulations of a partial differential equation (PDE) modeling propagation of electrical pulses on a one-dimensional ring of cardiac tissue are presented. The dynamics of the circulating pulse in this excitable medium are reduced to a single integral-delay equation. Stability conditions for steady circulation are obtained, and estimates are derived for the wavelength, growth rate, and asymptotic amplitude of oscillating solutions near the transition from steady rotation to oscillatory pulse dynamics. The analytical results agree with simulations of the delay equation and the PDE model and uncover previously uncharted solutions of the PDE equations.

Key words. delay equation, integral-delay equation, excitable media, reentry

AMS subject classifications. 35K57, 92C05

1. Introduction.

Excitable media can support self-sustained wave propagation on various geometries. Excitation pulses may circulate along a closed one-dimensional ring, rotate on a two-dimensional plane in the form of a spiral wave, or organize into scroll wave filaments in three-dimensional space. Most theoretical interest has focused on the study of spiral waves and scroll waves in excitable media, but there is not yet a good mathematical theory for the relatively simple problem of pulse circulation on a ring. This problem has concrete applications to experimental models of reentrant electrical activity in cardiac muscle.

In 1914, Mines [12] considered the circulation of an electrical pulse (or *action potential*) around a ring-shaped piece of atrial muscle dissected from tortoise heart. He proposed this preparation as a model for abnormal reentrant activity. Since then, the concept of reentry has evolved from the circulation of a pulse around an obstacle, often called *anatomical reentry*, to include *functional reentry* in the form of spiral waves [19, 18]. Recent experiments by Frame and Simson [4] on ring-shaped myocardial preparations dissected around the tricuspid valve orifice of dog hearts have provided detailed new results on the dynamics of pulse circulation in rings of living cardiac tissue. They looked at variations in action potential duration, circulation time, and other dynamical quantities during pulse circulation and described how these quantities relate to initiation and termination of the reentrant activity. They found that, in certain preparations, the magnitude of these quantities oscillated when measured once each rotation at a fixed point along the ring of tissue and that such oscillations often accompanied termination of reentrant propagation around the ring. Hence, an understanding of the nature of these oscillations could be helpful clinically in controlling the stability of anatomical reentry circuits.

* Received by the editors November 3, 1993; accepted for publication (in revised form) February 17, 1995. This research was partially supported by grants from the Heart and Stroke Foundation of Quebec and the Natural Sciences and Engineering Research Council of Canada. This work was included as part of the first author's Ph.D. thesis at the University of Arizona.

† Program in Applied Mathematics, University of Arizona, Tucson, AZ 85721, and Department of Physiology, McGill University, Montreal, Quebec H3G 1Y6, Canada. Current address, Research Center, Montreal Heart Institute, Montreal, Quebec, Canada H1T 1C8.

‡ Department of Mathematics, University of Utah, Salt Lake City, UT 84112. The research of this author was partially supported by National Science Foundation grant DMS9000588.

§ Department of Physiology, McGill University, Montreal, Quebec H3G 1Y6, Canada.

Our aim is to understand the dynamics of a propagating excitation pulse around a one-dimensional ring-shaped domain using a simple delay equation. In its most elaborate form, modeling of electrical propagation in cardiac tissue uses nonlinear partial differential equations (PDEs) that incorporate complex sets of equations to describe the electrical and ionic properties of cardiac cells [13, 11, 2]. In these continuous systems, oscillations similar to those observed by Frame and Simson arise when the circumference of the ring is made small enough. This instability has been shown in numerical studies by Quan and Rudy [13] and by Vinet and coworkers [16, 17] using modified Beeler–Reuter (BR) equations [1] and by Karma [9] using a two-variable system. Recently, Karma et al. [10] presented a theoretical analysis of the instability based on a direct reduction of the PDE model on a ring to a discrete map via a free-boundary problem formulation. To abstract the essential features of cardiac tissue that control its dynamics, theories based on finite-difference equations and spatially discrete models have also been developed based on mesoscopic properties such as the dispersion relation and the restitution curve [19, 15, 11, 7, 3].

The dispersion relation, $c(t_r)$, gives the dependence of the pulse propagation speed on the recovery time since the last pulse ended. The restitution curve, $a(t_r)$, gives the pulse duration as a function of the preceding recovery time. The recovery time (also called diastolic interval) at a point in the tissue is defined as the elapsed time between the onset of an excitation pulse and the end of the preceding pulse. It has been known for some time that the restitution curve can be used to construct a simple finite-difference equation describing the response of cardiac cells to periodic stimulation [5]. These results have shown that when the magnitude of the slope of the restitution curve exceeds unity at the predicted steady state, oscillations in pulse duration arise. Recently, Ito and Glass [7] presented a spatially discrete model of pulse propagation on a ring of tissue that uses the dispersion and restitution curves to predict pulse dynamics. Their work attempts to explain the experimental results of Frame and Simson [4] discussed above. They show good agreement between their discrete model and the experimental observations and link the onset of the pulse instability with the steepness of the restitution and dispersion curves at the steady state. The delay equation model presented here corresponds to a continuous-space limit of the discrete model introduced in [7].

In this study, we develop a theory about the nature of the pulse instability on the ring in both experimental preparations and numerical simulations of complex PDEs based on a single *continuous* integral-delay equation (IDE). The continuous IDE allows us to carry out analytical computations not previously obtained with discrete models. We examine in detail the onset of nonsteady circulation using the BR equations on a one-dimensional ring. Destabilization of steady propagation occurs as the circumference of the ring is reduced, leading to oscillations in the pulse speed, pulse duration, and recovery time with a wavelength slightly less than twice the ring length. The dynamics of pulse circulation on a ring can be reduced to an IDE using the dispersion and restitution curves. This is done directly in the case of a general two-variable model. We find a simple criterion for pulse stability based solely on the steepness of the restitution curve, but in addition, the IDE provides novel information about the nature of the bifurcation and of the oscillatory solutions that arise from it (number, wavelength of unstable modes, amplitude of periodic solutions). Analytical results from the delay equation can be used to predict numerical results for both the IDE and more complex PDE system. In addition, the IDE predicts previously uncharted solutions that can be observed in the PDE with appropriate

initial conditions. This work extends the results presented in our earlier preliminary report [3].

2. The PDE model. In this section, we present numerical results from simulations of pulse circulation on a ring, using the BR equations to represent the electrical properties of the medium. The phenomena observed in the full PDE model will then be described and analyzed later in terms of a simple delay equation.

2.1. Equation and numerical methods. The BR equations are incorporated in a reaction-diffusion PDE model of cardiac electrical activity, also known as the cable equation. On a one-dimensional ring, we use a forward Euler method to integrate

$$\frac{\partial V}{\partial t} = -\frac{I_{BR}(V)}{C_m} + D\frac{\partial^2 V}{\partial x^2}, \quad 0 \le x \le L \quad \text{and} \quad V(0) = V(L), \tag{1}$$

where V is the cardiac cell membrane voltage (mV), $D = (C_m S_v \rho)^{-1}$ is the diffusion coefficient, $C_m = 1.0$ μF cm^{-2} is the membrane capacitance, $S_v = 5000$ cm^{-1} is the surface-to-volume ratio of the cardiac cells, and $\rho = 0.2$ kΩ cm is the longitudinal tissue resistivity of cardiac muscle. I_{BR} is the total membrane current obtained from the BR equations (μA cm^{-2}) and is given as a function of V only to simplify the notation. The BR equations [1] consist of seven time- and voltage-dependent variables used to describe four membrane currents carried by sodium, potassium, and calcium ions, which are added up to produce the total current I_{BR}. The BR equations, needed to complete (1), are given in detail in the appendix. Our numerical method yields a difference equation for the voltage V at location $i\triangle x$ and time $(n+1)\triangle t$ of the form

$$V_i^{n+1} = V_i^n + \triangle t \left(\frac{I_{BR}(V_i^n)}{C_m} + \frac{1}{C_m S_v \rho} \frac{V_{i+1}^n - 2V_i^n + V_{i-1}^n}{\triangle x^2} \right). \tag{2}$$

The integration is performed using a fixed spatial discretization step $\triangle x = 0.025$ cm and a fixed temporal discretization step $\triangle t = 0.025$ ms. Refining the spatial and temporal discretization steps leads to a faster propagation velocity (about 10% faster for planar waves in recovered medium with $\triangle x = 0.01$ cm and $\triangle t = 0.01$ ms) but does not modify the qualitative nature of the solutions as the ring length is reduced. This was checked explicitly for all computations presented in this study.

A circulating pulse is obtained by stimulating the proximal end of a long cable ($L = 15$ cm) to obtain a propagating action potential. As the activation front approaches the distal end of the cable, the two ends of the cable are joined numerically into a ring. After stabilization of the pulse, the ring size is decreased in successive steps by splicing out part of the ring. Gridpoints are removed starting 10 grid locations behind the excitation front (marked by $V = -60$ mV and $\partial V/\partial t > 0$) during the action potential. Increases in ring length are obtained by inserting gridpoints 10 grid locations behind the front. The new points are assigned state values from one of the adjacent points. We measure the pulse duration A, the speed C, the recovery time t_r, and the circulation time T as the pulse propagates along the ring (this is explained further below), using -60 mV as our threshold between the recovered state ($V < -60$ mV) and the excited state ($V \ge -60$ mV). Speeds are calculated using the propagation time of the wavefront over a distance of $3\triangle x$.

2.2. PDE simulation results. Stable circulation becomes unstable in the PDE model as L is decreased below $L = 13.4$ cm. At $L = 13.4$ cm there is stable circulation

with $C \approx 0.0415$ cm/ms, $A \approx 211$ ms, and $t_r \approx 112$ ms. During stable circulation, all three quantities reach constant steady-state values as the pulse circulates around the ring. We have examined in detail the behavior of solutions as the ring length is decreased from $L = 13.4$ cm to $L = 13.15$ cm. Starting from the stable solution at $L = 13.4$ cm, we gradually decrease the ring length, one gridpoint at a time, allowing 40 rotations at each ring length. At any given ring length, if the dynamics have not stabilized after 40 rotations, the simulations are continued until transients have dissipated. In the end, simulations were carried out for at least 150 rotations at each ring length.

In order to adequately display the dynamics of unstable solutions, we plot the changes in A, C, t_r, and T as a function of the location x of the wavefront along the ring. The space-time diagram of Fig. 1, which displays the oscillating solution observed at $L = 13.15$ cm, illustrates how we compute these quantities. Each trace in the figure is a plot of the potential V as a function of distance along the ring at a fixed time. Each plot is repeated once horizontally to highlight continuity at the boundary. Traces are stacked vertically at the rate of one every 10 milliseconds. We define a time-dependent coordinate $x(t)$ corresponding to the location of the wavefront along the ring. This coordinate increases continuously as the front circulates around the ring. Two values x and x' are identified with the same location on the ring if $x \bmod L = x' \bmod L$. In Fig. 1, assuming that the first trace is taken at $t = 0$ (bottom trace), the trace whose excitation front is labeled with an asterisk corresponds to $t = 400$ ms. Let x^* be the location of the labeled wavefront as described above; then we define four quantities: $C(x^*)$ is the speed of the excitation front at x^*, $A(x^*)$ is the duration of the pulse that is just beginning when the front reaches x^*, $t_r(x^*)$ is the recovery time that is just ending as the front reaches x^*, and $T(x^*)$ is the circulation time from $x^* - L$ to x^*.

Between $L = 13.4$ cm and $L = 13.2$ cm, there is either a stable steady state or small oscillations in $t_r(x)$ upon gradually decreasing the ring circumference. Figure 2 shows traces of $t_r(x)$ for ring lengths in this range after transients have dissipated. For some ring lengths, transients were extremely long, up to 300 rotations in certain cases (e.g., $L = 13.2$ cm). Below $L = 13.2$ cm, the amplitude of the oscillations increases dramatically. At $L = 13.175$ cm, the solution showed oscillations whose amplitude increased gradually. Over 600 rotations were required for the solution to reach its asymptotic peak-to-peak amplitude of 160 ms. At $L = 13.15$ cm, the oscillating solution quickly increased to its stable large amplitude.

There is hysteresis in the dynamics upon *increasing* the ring length from $L = 13.15$ cm. The large amplitude oscillations are maintained as the ring length is increased from $L = 13.15$ cm to $L = 13.3$ cm. Starting from the solution at $L = 13.15$ cm, we increased the ring length one gridpoint at a time, allowing 100 rotations between increases in ring length. The simulations were then extended for another 200 rotations at each ring length. The peak-to-peak amplitude of the oscillations decreased from 164 ms at $L = 13.15$ cm to 122 ms at $L = 13.3$ cm. Between $L = 13.2$ cm and $L = 13.3$ cm, the high-amplitude solutions differed markedly from the low-amplitude solutions of Fig. 2. There appears to be bistability within this region. Above $L = 13.3$ cm, the solutions are as depicted in Fig. 2.

When examined as a function of the time-dependent coordinate x, we find that destabilization of the steady-state leads to periodic solutions for A, C, t_r, and T whose wavelengths are slightly less than twice the ring length. As the ring length is decreased, the amplitude of the oscillations increases and their wavelength decreases. Figure 3 shows traces of $C(x)$, $A(x)$, $t_r(x)$, and $T(x)$ for the oscillating solution at

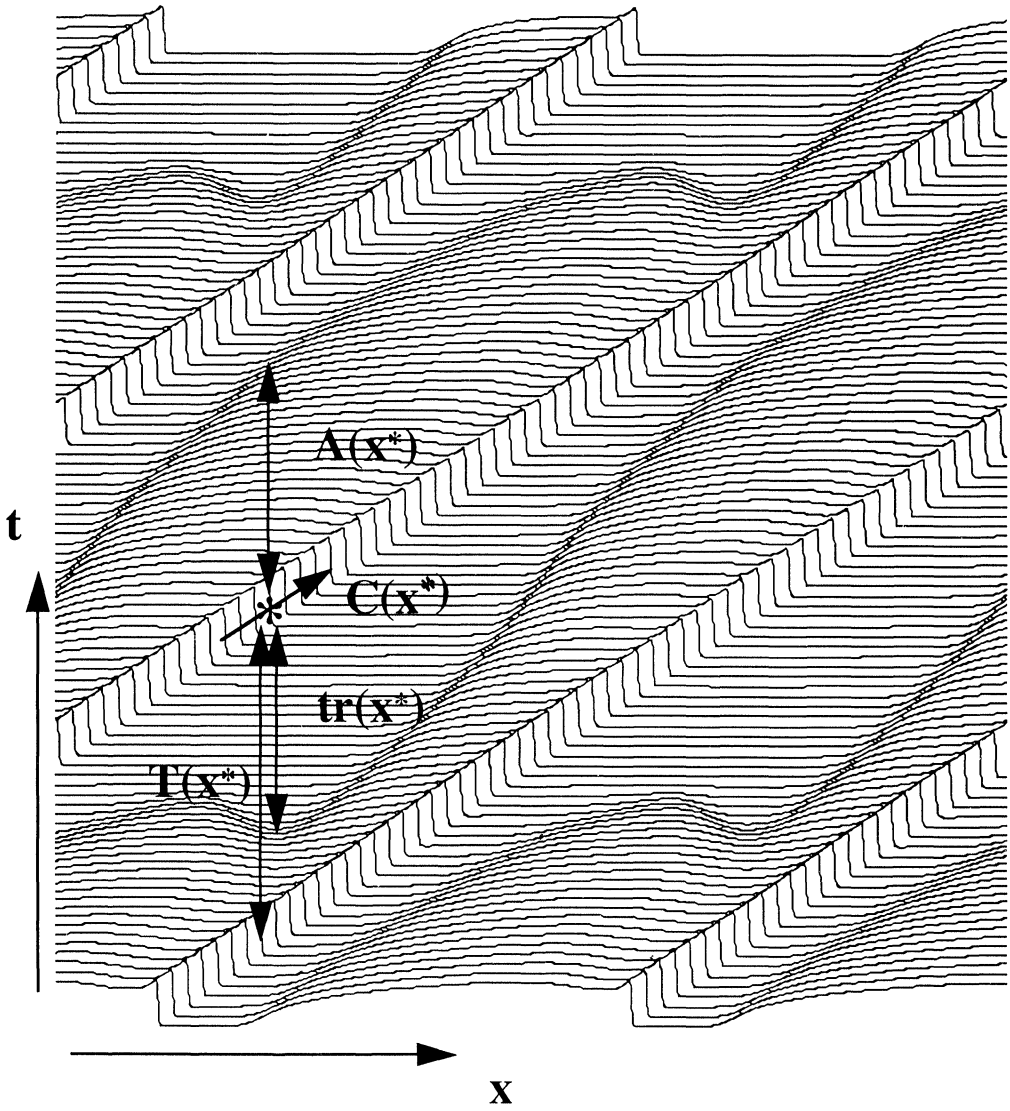

FIG. 1. *Dynamics of a circulating pulse on a ring of length* $L = 13.15$ *cm found from numerical integration of the BR equations. Each horizontal trace represents the profile of voltage along the ring, repeated once to illustrate continuity. Traces are then stacked vertically once every* 10 *ms (time increases from bottom to top). Note the large changes in pulse duration as the excitation propagates from left to right along the ring. At a given location of the excitation front along the ring, labeled with an asterisk* ($x = x^*$)*, we illustrate the quantities we use to characterize the dynamics of the circulating pulse, namely the pulse speed* $C(x^*)$*, the pulse duration* $A(x^*)$*, the recovery time* $t_r(x^*)$*, and the circulation time* $T(x^*)$.

$L = 13.15$ cm. The wavelength of the oscillation is $\Lambda = 25.8$ cm. The values of A, t_r, and C oscillate in phase, while the circulation time T is 90 degrees out of phase. The relative amplitudes of the oscillations in A and t_r are similar. Because the wavelength is not exactly twice the ring length, the dynamics of C, A, t_r, and T at any fixed location on the ring are *quasiperiodic* in time. Figure 4 shows the sequence

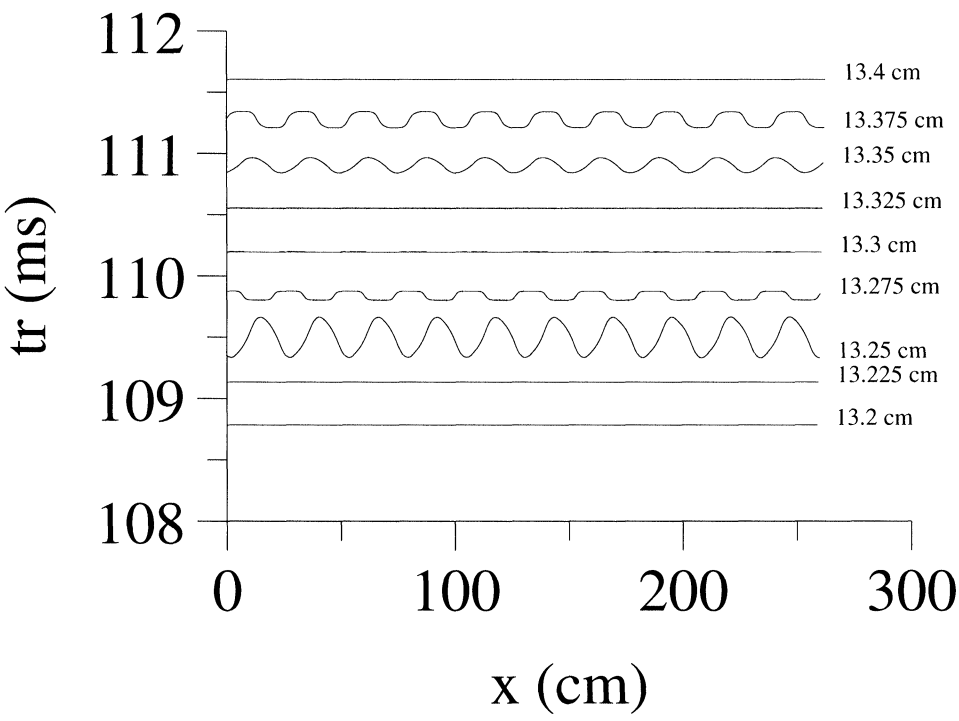

FIG. 2. *Dynamics of a circulating pulse on rings of increasing size starting at* $L = 13.4$ *cm. Ring length is reduced by one gridpoint* (0.025 *cm*) *every* 40 *pulse rotations. The simulations are then extended at each ring length until transients are dissipated. The recovery time* $t_r(x)$ *is plotted for* 9 *ring lengths starting at* $L = 13.4$ *cm and ending at* $L = 13.2$ *cm, after at least* 150 *rotations at each ring length (up to* 330 *rotations as required to dissipate transients).*

of recovery times t_r and circulation periods T measured during consecutive turns at a fixed location along the ring.

Sustained circulating pulses are observed on rings as small as 12 cm. The minimal ring length that will support circulation seems to fall between $L = 12$ cm and $L = 11$ cm. Figure 5 shows traces of $C(x)$, $A(x)$, $t_r(x)$, and $T(x)$ at $L = 12$ cm, where the oscillations have nearly reached their largest amplitude. Figure 6 shows a tracing of the membrane voltage V as a function of time obtained at a fixed location along the ring, again at $L = 12$ cm. Alternations in the duration of the successive electrical pulses can be observed. The complex appearance of the pulse dynamics in this plot can be distilled into the simple periodic solutions of Fig. 5. These results on the ring geometry are in accord with experimental observations by Frame and Simson [4]. They demonstrated the onset of oscillations during pulse circulation in a loop of cardiac tissue and obtained oscillations that appeared quasi-periodic in time, as in the plot of Fig. 4.

3. The delay equation. In this section, we develop a continuous theory for pulse propagation on a ring by deriving a simple governing equation using the dispersion and restitution curves. Using the quantities $A(x)$, $t_r(x)$, and $C(x)$ we may write an equation stating that, for any point x along the ring, the recovery time is

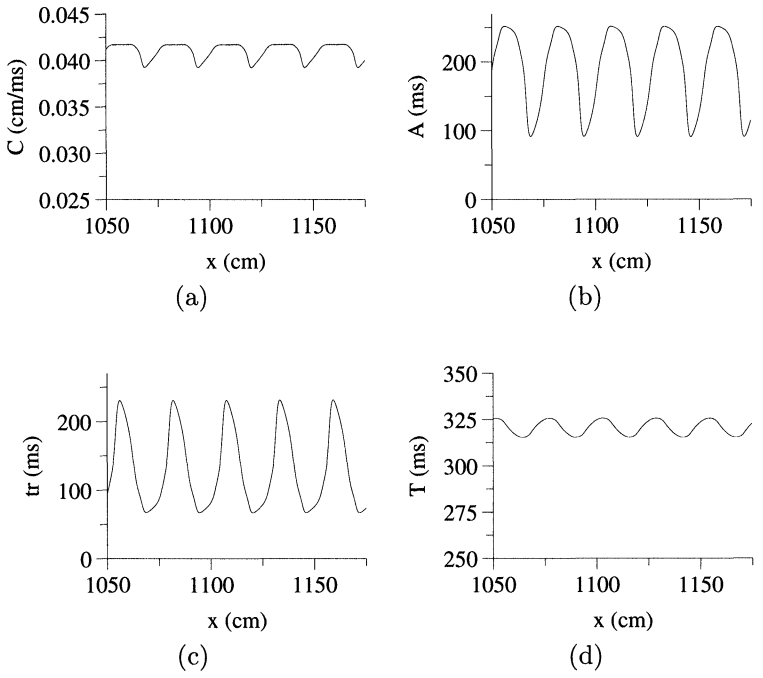

FIG. 3. *Dynamics of a circulating pulse on a ring of length* $L = 13.15$ *cm found from numerical integration of the BR equations.* (a) *Speed* $C(x)$, (b) *pulse duration* $A(x)$, (c) *recovery time* $t_r(x)$, (d) *circulation period* $T(x)$. *Transients have dissipated. Wavelength is* $\Lambda = 25.8$ *cm.*

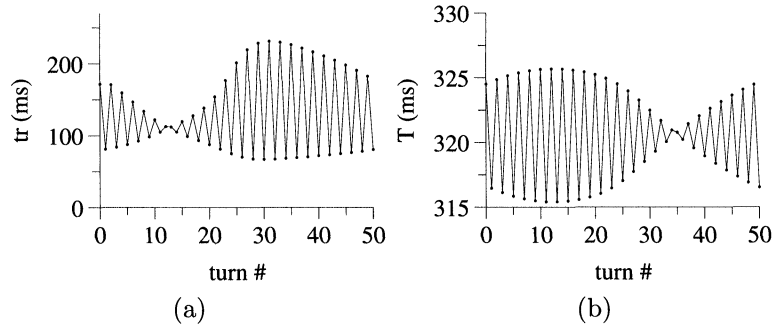

FIG. 4. *Dynamics of a circulating pulse in a ring of length* $L = 13.15$ *cm found from numerical integration of the BR equations. Plot of* (a) *the recovery time* t_r *and* (b) *the circulation period* T *as a function of the number of turns around the ring at a fixed location.*

the difference between the circulation time and the pulse duration. From Fig. 1, we see that

$$T(x) = t_r(x) + A(x - L). \tag{3}$$

Substituting $\int_{x-L}^{x} ds/C(s)$ for the circulation time $T(x)$ yields the equation

$$t_r(x) = \int_{x-L}^{x} \frac{ds}{C(s)} - A(x - L). \tag{4}$$

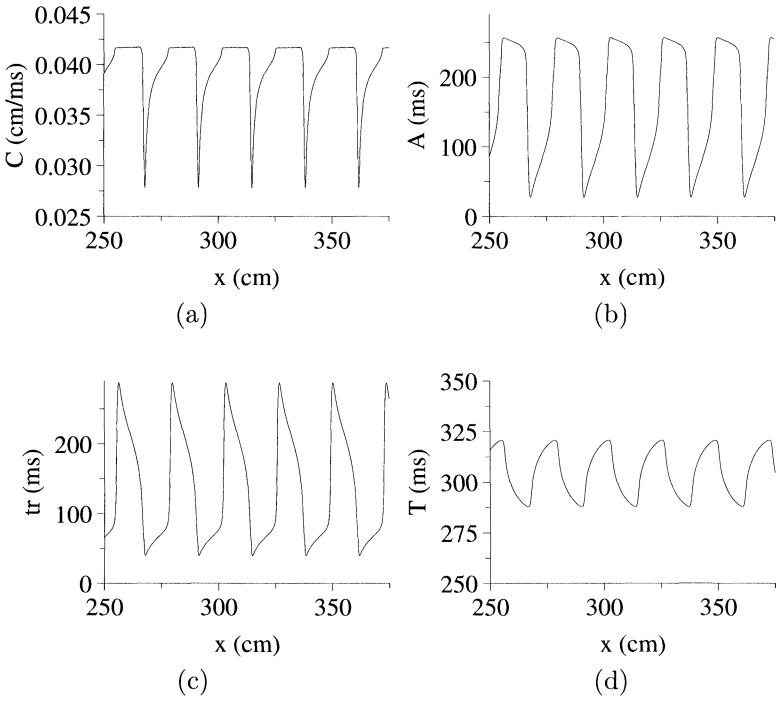

FIG. 5. *Dynamics of a circulating pulse on a ring of length* $L = 12.0$ *cm found from numerical integration of the BR equations.* (a) *Speed* $C(x)$, (b) *pulse duration* $A(x)$, (c) *recovery time* $t_r(x)$, (d) *circulation period* $T(x)$. *Transients have dissipated. Wavelength is* $\Lambda = 23.5$ *cm.*

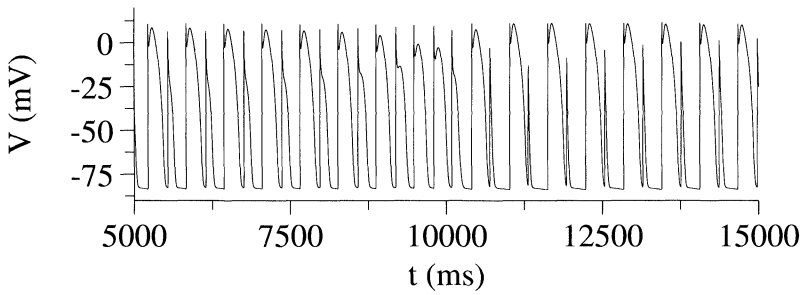

FIG. 6. *Trace of voltage (in mV) versus time (in ms) from a fixed location on the ring during pulse circulation using the BR equations. This time series is taken from a simulation at* $L = 12$ *cm. The trace illustrates the quasi-periodic oscillations in the duration of the successive excitation pulses.*

Our theory is based on the assumption that both the pulse duration and the speed can be expressed as functions of the recovery time t_r. The function $a(t_r)$, describing the relation between A and t_r, is called the *restitution curve*, while $c(t_r)$ is called the *dispersion curve*. The assumption that both curves are well-defined unique functions of t_r is common in the analysis of cardiac propagation [15, 13, 11, 7, 8] and is satisfied in excitable media, where the time course of recovery (and its effect on the response

of the system to excitation) does not depend on past history of the system. In other words, we assume that recovery occurs along a one-dimensional slow manifold, typical of simple two-variable caricatures of excitable media. The IDE also assumes that the effect of diffusion can be restricted to a boundary layer in the vicinity of the excitation front, thereby treating the excitation process as a sharp front. We show how one can derive expressions for the restitution and dispersion curves, and hence the IDE, directly from a general two-variable model of an excitable system below. The derivation highlights the assumptions involved in extending this theory to the more complex BR equations.

3.1. The IDE in a two-variable model. Consider the system of equations

$$\epsilon \frac{\partial u}{\partial t} = \epsilon^2 \frac{\partial^2 u}{\partial x^2} + f(u,v), \qquad \frac{\partial v}{\partial t} = g(u,v), \tag{5}$$

where f and g are typical functions describing an excitable medium, e.g., the cubic and linear functions of the FitzHugh–Nagumo model. The equation $f(u,v) = 0$ has three solutions, denoted $u = U_-(v)$, $U_0(v)$, and $U_+(v)$, with $U_-(v) \le U_0(v) \le U_+(v)$ wherever comparison is possible. We assume that $U_-(v)$ exists only for $v \ge v_-$, and $U_+(v)$ exists only for $v < v_+$. The solution branch with $u = U_+(v)$ is commonly called the excited branch, and the branch with $u = U_-(v)$ is called the recovering branch. The function $f(u,v)$ is positive for u sufficiently large and v sufficiently negative, the function $g(u,v)$ is positive for large positive u and large negative v, and the nullcline $g(u,v) = 0$ has a single intersection with the curve $u = U_-(v)$, so there is a unique stable rest point for the system (5).

We use singular perturbation theory to understand the behavior of the system (5) in the limit where $0 < \epsilon \ll 1$. Simply setting $\epsilon = 0$, we obtain the "outer equation"

$$\partial v/\partial t = g(u,v), \qquad f(u,v) = 0. \tag{6}$$

The two stable roots of $f(u,v) = 0$ are denoted $u = U_\pm(v)$, so the outer dynamics become

$$\partial v/\partial t = g(U_\pm(v), v) = G_\pm(v), \tag{7}$$

where the $+$ dynamics are followed on the excited branch and the $-$ dynamics are followed on the recovering branch.

Outer dynamics fail in some regions of space and must be patched together with moving transition layers within which

$$u(x,t) = U\left(\frac{x - Ct}{\epsilon}\right), \qquad v(x,t) = V\left(\frac{x - Ct}{\epsilon}\right). \tag{8}$$

A simple change to moving coordinates shows that to leading order in ϵ, U and V satisfy

$$U'' + CU' + f(U,V) = 0, \qquad V = v_0 \tag{9}$$

and that to match with the outer solution it must be that $\lim_{\xi \to \pm\infty} f(U(\xi), v_0) = 0$. This implies that $C = \lambda(v_0)$ is a nonlinear eigenvalue, which is known to exist and be unique.

Now we may piece together the following scenario. The speed at which the excitation propagates is $\lambda(v_e)$, where $v_e(x)$ is the V level at which the excitation occurred. We also assume that the recovery is always via a phase wave, so that recovery always takes place at $v_r = v_+$.[1] Now, we define the action potential duration as the time spent on the excited branch,

$$A(x) = \int_{v_e}^{v_+} \frac{dv}{G_+(v)} = F_1(v_e), \tag{10}$$

and the recovery time preceding excitation as

$$t_r(x) = \int_{v_+}^{v_e} \frac{dv}{G_-(v)} = F_2(v_e). \tag{11}$$

The function $G_-(v)$ is negative on the recovery branch, so the equation above can be reexpressed as

$$v_e = F_2^{-1}(t_r). \tag{12}$$

Now we can write the pulse duration and speed as a function of t_r,

$$A = F_1(F_2^{-1}(t_r)) = a(t_r), \qquad C = \lambda(F_2^{-1}(t_r)) = c(t_r), \tag{13}$$

thereby defining the restitution and dispersion curves.

Using the restitution and dispersion curves, (4) may be rewritten as

$$t_r(x) = \int_{x-L}^{x} \frac{ds}{c(t_r(s))} - a(t_r(x-L)), \tag{14}$$

which is an IDE for the recovery time t_r. It completely describes the dynamics of pulse circulation on the ring.

Equation (14) can be reduced to a neutral differential-delay equation [6] by taking derivatives with respect to x, which yields

$$\frac{d}{dx}\left(t_r(x) + a\left(t_r(x-L)\right)\right) = \frac{1}{c\left(t_r(x)\right)} - \frac{1}{c\left(t_r(x-L)\right)}. \tag{15}$$

We used the form of (15) in [3]. We shall use the IDE in what follows.

3.2. Restitution and dispersion in the BR model. We cannot derive the restitution and dispersion relations analytically from the BR equations. Our assumption that these two curves are unique and well defined in the PDE model can be tested by computing dispersion and restitution curves for the BR model and comparing simulation results from the PDE and IDE models. In Fig. 7 we plot pulse duration and speed as functions of t_r, based on data from the simulation at $L = 13.15$ cm and $L = 12.0$ cm in Figs. 3 and 5. At each location x along the ring, the values of A, C, and t_r can be obtained and plotted against one another (bold dots in Fig. 7). Our assumption requires that the restitution and dispersion curves be independent of the

[1] In general this is incorrect, but it serves as an adequate first approximation here. A more accurate estimate of v_r could be obtained by considering the recovery process as a propagating front and requiring that its speed, $-\lambda(v_r)$, equal the excitation front speed, $\lambda(v_e)$.

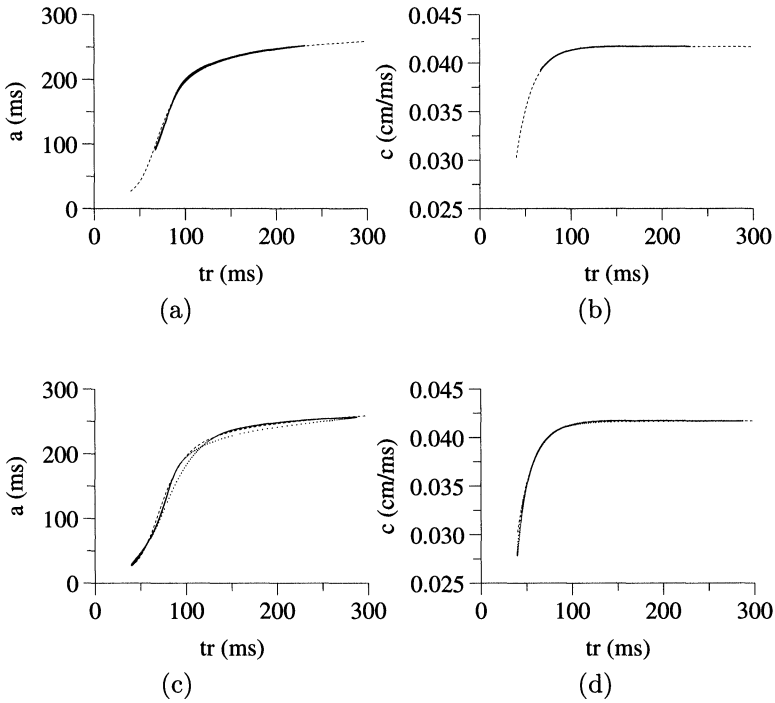

FIG. 7. (a) *Restitution curve* $a(t_r)$ *and* (b) *dispersion curve* $c(t_r)$ *derived from the pulse circulation in Fig.* 3. (c) *Restitution curve* $a(t_r)$ *and* (d) *dispersion curve* $c(t_r)$ *derived from the pulse circulation in Fig.* 5. *There is splitting of the restitution curves that is more pronounced in* (c), *corresponding to larger oscillations in* A *and* t_r *in Fig.* 5. *The splitting is due to hysteresis in the pulse duration depending on whether the recovery time increases or decreases. The dashed curves displayed on each panel shows the final fitted version of the curves to be used in the analysis.*

ring length and previous history of the medium and that they both be well-defined single-valued functions of t_r. The curves of Fig. 7 are similar, except that there is a splitting of the restitution curve that is more pronounced at the shorter ring length. This is due to hysteresis in the response of the system depending on whether the recovery time t_r is increasing or decreasing and shows that our slow-manifold assumption is not completely satisfied.

It is possible to measure the restitution and dispersion curves under different conditions. For example, we could measure the restitution curve using external stimuli applied to the spatially uniform BR model ($D = 0$ in (1)). A curve obtained in this fashion would be different from the restitution curve of Fig. 7. First, an action potential triggered by an external stimulus is different from one arising as a result of propagation. Second, there are spatial diffusive influences affecting propagating pulses which are not present in the spatially uniform case. Similarly, we could obtain a dispersion relation by writing a simplified ordinary differential equation equation in the form of (9) for the PDE system and solving the equation numerically. This can be carried out analytically in some simple piecewise linear two-variable systems, as shown in Rinzel and Keller [14]. Because we did not observe splitting of the dispersion relations in Fig. 7, we believe that such a "steady-state" curve would not be significantly different from the relationship obtained from the PDE simulation

data, except for the effect of the PDE discretization on the wave speed. By choosing to obtain our restitution curve from the pulse circulation data, we are bypassing a weakness in the present theory.

In what follows, we assume that the relations at both ring lengths can be represented by unique well-defined functions of t_r. We fit the data of Fig. 7 with the equations

$$\begin{aligned} a(t_r) &= 20 + B(t_r)t_r^{5.5}/(72^{5.5} + t_r^{5.5}), \text{ where } B(t_r) = 250 - 90e^{-t_r/145}, \\ c(t_r) &= 0.0417 - 0.0135e^{-(t_r-37)/18}, \end{aligned} \tag{16}$$

where the units of time are milliseconds and the units of space are centimeters. The curves of (16) are plotted as dashed lines in the panels of Fig. 7. The deviation between the fitted and numerical dispersion curves is small, as can be seen in panels (b) and (d). For the restitution curves, the largest deviations are found in Fig. 7(c) and can reach 10%–15% of the pulse duration at their maximum. The fitting procedure emphasized a close fit to the data of panel (a), instead of attempting to average across the hysteresis found in the data of panel (c). For the dispersion relations, we assume that pulse propagation is impossible for $t_r < 37$ ms. This is a feature of excitable media wherein pulse trains become unstable at a finite frequency corresponding to a finite nonzero wavespeed. We use the analytical expressions in (16) to compute quantities relating to the restitution and dispersion curves in the remainder of this paper.

3.3. Analysis of the IDE. In this section we present some analytical results about the dynamics of the IDE. The stability region of the steady state is identified using linear stability analysis. We show that the steady state loses stability through an infinite-dimensional Hopf bifurcation when the slope of the restitution curve exceeds one at the steady state. Using perturbation methods, estimates for the frequency and growth rate of the unstable oscillating modes are computed near the bifurcation. We end this section by carrying out nonlinear analysis of the IDE to obtain estimates for the amplitude of oscillating solutions beyond the bifurcation.

Before pursuing the analysis, it is convenient to change variables in (14). Setting $y = Qx/L$ and $t_r(Ly/Q) = z(y)$ into (14) yields

$$z(y) = \frac{1}{Q}\int_{y-Q}^{y} d(z(s))ds - a(z(y-Q)), \tag{17}$$

where $d(z) = L/c(z)$. Equation (17) has steady-state solutions $z = z*$ satisfying

$$z^* = d(z^*) - a(z^*). \tag{18}$$

3.3.1. Linear stability. Let $a' = \mathbf{d}a/\mathbf{d}z(z^*)$ and $d' = \mathbf{d}d/\mathbf{d}z(z^*)$. Linearizing (17) near $\tilde{z}(y) = z(y) - z^* = 0$ yields

$$\tilde{z}(y) = \frac{1}{Q}\int_{y-Q}^{y} d'\tilde{z}(s)ds - a'\tilde{z}(y-Q). \tag{19}$$

We look for solutions to (19) of the form $\tilde{z} = Ce^y$. In the original coordinates, these solutions are of the form $t_r = t_r^* + be^{Qx/L}$, so that Q/L is an eigenvalue of the linearized integral equation (14). Substituting for $\tilde{z}$ in (19) gives

$$Q(1 + a'e^{-Q}) = (1 - e^{-Q})d'. \tag{20}$$

The stability of the steady state is determined by the roots of (20), which is the characteristic equation for the IDE. Stability requires $\Re(Q) < 0$, where $\Re(Q)$ and $\Im(Q)$ represent the real and imaginary parts of Q, respectively. There is a loss of stability of the steady state when the roots cross from the left to the right complex plane, indicated by $\Re(Q) = 0$. Given that both the restitution and dispersion curves are monotonically increasing functions of the recovery time, we limit ourselves to the case where $a' \geq 0$ and $d' < 0$.

THEOREM. *Let $Q \neq 0$ be a nontrivial root of* (20) *for $a' \geq 0$, $d' < 0$; then* $\Re(Q) = 0 \iff a' = 1$, $\Re(Q) < 0 \iff 0 \leq a' < 1$, $\Re(Q) > 0 \iff a' > 1$.

Proof. We begin by rearranging (20) to obtain

$$e^{-Q}(d' + a'Q) = d' - Q. \tag{21}$$

Equating norms, we get

$$|e^{-Q}||d' + a'Q| = |d' - Q|. \tag{22}$$

Let $\Re(Q) = 0$; then $|e^{-Q}| = 1$ and (22) implies $a'^2 = 1$, which yields $a' = 1$ for $a' \geq 0$. Now let $a' = 1$. Assume $\Re(Q) > 0$; then $|e^{-Q}| < 1$ and (22) implies $|d' + Q| > |d' - Q|$. This is a contradiction since $|d' + Q| < |d' - Q|$ for $\Re(Q) > 0$ and $d' < 0$. Next assume $\Re(Q) < 0$; then $|e^{-Q}| > 1$ and (22) implies $|d' + Q| < |d' - Q|$. This is a contradiction since $|d' + Q| > |d' - Q|$ for $\Re(Q) < 0$ and $d' < 0$. Hence, $a' = 1$ implies $\Re(Q) = 0$, and we have shown that $a' = 1 \iff \Re(Q) = 0$.

Let $\Re(Q) > 0$; then $|e^{-Q}| < 1$ and (22) implies $|d' + a'Q| > |d' - Q|$. Assume $0 \leq a' < 1$; then $|d' + a'Q| < |d' - Q|$ for $\Re(Q) > 0$ and $d' < 0$, and we have a contradiction. Hence if $\Re(Q) > 0$ and $a' \geq 0$, we must have $a' > 1$. Now let $a' > 1$. We have shown above that $\Re(Q) \neq 0$. Assume $\Re(Q) < 0$; then $|e^{-Q}| > 1$ and (22) implies $|d' + a'Q| < |d' - Q|$. This is a contradiction since $|d' + a'Q| > |d' - Q|$ for $\Re(Q) < 0$, $d' < 0$, and $a' > 1$. Hence, $a' > 1$ implies $\Re(Q) > 0$, and we have shown that $a' > 1 \iff \Re(Q) > 0$. The above argument is easily reversed to show that $0 \leq a' < 1 \iff \Re(Q) < 0$, which completes the proof.

The theorem gives the stability region of the steady state for $a' \geq 0$ and $d' < 0$. Stability for $0 \leq a' < 1$ is lost at $a' = 1$ through an infinite-dimensional Hopf bifurcation. Figure 8 follows the trajectory of $Q^{(0)}$ in the complex plane as a' is varied from -1 to 1, keeping $d' < 0$ fixed. At $a' = -1$, the root crosses the imaginary axis into the left-hand plane near $2\pi i$. It then curves around and crosses the imaginary axis into the right-hand plane near πi. This behavior appears typical of all roots $Q^{(k)}$ and occurs symmetrically across the real axis. For $d' < 0$ and $a' < 0$, there is an additional real root that crosses from the left to the right complex plane when $a' = -1 + d'$. We have not considered here the more complicated behavior of roots in the case $d' > 0$.

Our application to excitable media sets $a' \geq 0$ and $d' < 0$. We are particularly interested in the bifurcation at $a' = 1$, where we find that the imaginary part q_0 of the roots satisfies

$$\tan\left(\frac{q_0}{2}\right) = \frac{q_0}{d'}. \tag{23}$$

The solutions of (23) can be viewed graphically as the intersection between the straight line of slope $1/d'$ and the tangent function. There are an infinite number of solutions (this is true in general for (20)) associated with an infinite number of roots $Q^{(k)} = iq_0^{(k)}$

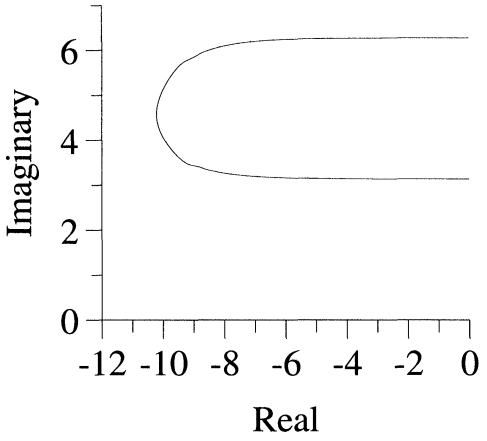

FIG. 8. *Dependence of the root $Q^{(0)}$ of (20) on the value of a' as it varies from -1 to 1, keeping d' fixed (here $= -0.001$). The root enters the left complex half-plane near $2\pi i$ at $a' = -1$ and leaves it near πi at $a' = 1$. Note that the imaginary axis is along the right edge of the figure.*

crossing the imaginary axis. If we assume that the dispersion relation is nearly flat at the bifurcation point, then $|d'| \ll 1$, and the imaginary parts $q_0^{(k)}$ of the roots can be approximated as

$$q_0^{(k)} = (2k+1)\pi - \frac{2d'}{(2k+1)\pi} + \mathcal{O}(d'^2), \quad k = 0, 1, 2, \ldots. \tag{24}$$

For the BR equations, we have $d' \approx -0.088$ at the bifurcation.

3.3.2. The characteristic equation near the bifurcation. Given that an infinite number of unstable modes exist for $a' > 1$, we carry out an expansion of the roots of (20) for a' close to 1 to find the relative growth rates of the modes near the bifurcation. We set $a' = 1 + \epsilon$, keep d' fixed, and assume $Q^{(k)}$ has a power series expansion of the form

$$Q^{(k)} = iq_0^{(k)} + \epsilon q_1^{(k)} + \epsilon^2 q_2^{(k)} + \mathcal{O}(\epsilon^3), \tag{25}$$

where $q_0^{(k)}$ is one of the solutions of (23). We drop the (k) index on q_0 for the remainder of this section. Substituting into (20), expanding into powers of ϵ, and solving term by term, we find

$$q_1^{(k)} = \frac{q_0^2}{d'^2 - 2d' + q_0^2} + i\frac{q_0 d'}{d'^2 - 2d' + q_0^2}. \tag{26}$$

The characteristic equation (20) assumes solutions of the form $t_r(x) = t_r^* + be^{Qx/L}$, so that the predicted growth rate of the kth mode near the bifurcation is

$$t_r(x) \sim \exp\left(\epsilon \frac{q_0^2}{d'^2 - 2d' + q_0^2} \frac{x}{L}\right). \tag{27}$$

For $|d'| \ll 1$, using (24), $q_1^{(k)}$ simplifies to

$$q_1^{(k)} = \left(1 + \frac{2d'}{(2k+1)^2\pi^2}\right) + i\frac{d'}{(2k+1)\pi} + \mathcal{O}(d'^2), \quad k = 0, 1, 2, \ldots, \tag{28}$$

so that the growth rate of the kth mode becomes

$$\exp\left(\epsilon\left(1+\frac{2d'}{(2k+1)^2\pi^2}\right)\frac{x}{L}\right). \tag{29}$$

Near the bifurcation, the linear growth of the unstable modes near the steady state is lowest for the lowest-frequency components. In particular, the slowest frequency at $q_0^{(0)}$ grows the slowest initially. The wavelength of the unstable modes, for $|d'| \ll 1$, is given by

$$\Lambda^{(k)} = \frac{2\pi L}{\Im(Q)} = \frac{2L}{2k+1} + \frac{2d'L(2-\epsilon)}{(2k+1)^3\pi^2} + \mathcal{O}(d'^2). \tag{30}$$

The mode of lowest frequency, $\Lambda^{(0)}$, has wavelength slightly less than twice the ring length. The linear theory does not suggest dominance of this mode over the others based on its initial growth rate.

3.3.3. Nonlinear analysis near the bifurcation. In order to get an estimate of the asymptotic amplitude of oscillating solutions beyond the Hopf bifurcation at $a' = 1$, we look for small-amplitude periodic solutions of (14). We rewrite (17) as

$$z(y) = \frac{L}{L_0 Q}\int_{y-Q}^{y} D(z(s))ds - a(z(y-Q)), \tag{31}$$

where $D(z) = L_0/c(z)$, and pick L_0 so that $a' = 1$ at $L = L_0$.

To find nontrivial periodic solutions in a neighborhood of L_0, we use L/L_0 as a bifurcation parameter. By picking Q so that the solutions are 2π-periodic in y, the ratio of the wavelength of the solutions to the length of the loop L is $\Lambda/L = 2\pi/Q$. Hence Q is the relative wavenumber. At the bifurcation point, we pick $Q = iq_0$. We expand $a(z)$ and $D(z)$ into local power series about z^* of the form

$$a(z) = a(z^*) + a_1(z-z^*) + a_2(z-z^*)^2 + \cdots, \tag{32}$$

$$D(z) = d_0 + d_1(z-z^*) + d_2(z-z^*)^2 + \cdots, \tag{33}$$

where $a_1 = a' = 1$, $d_0 = D(z^*)$, and $d_1 = d'$. Taking $Q = iq_0 + \epsilon^2 q_2 + \cdots$ and $L/L_0 = 1 + \epsilon^2\lambda_2$, we substitute for a, D, Q, and L/L_0 into (31) and solve the resulting equations for powers of ϵ assuming solutions of the form

$$z(y) = z^* + \epsilon(Me^{iy} + \overline{M}e^{-iy}) + \mathcal{O}(\epsilon^2), \tag{34}$$

where $\overline{M}$ denotes the complex conjugate of M. The solvability condition at $\mathcal{O}(\epsilon^3)$ yields the relation[2]

$$0 = 2\lambda_2 q_0^2 a_2 d_0 + M\overline{M}(-3a_3q_0^2(d_1-2) + a_2^2(3d_1^3 - 6d_1^2 + q_0^2 d_1 - 6q_0^2) + 2a_2d_2(-3d_1^2 + 6d_1 + 2q_0^2)). \tag{35}$$

This equation gives an approximation for the solution amplitude as a function of the bifurcation parameter L/L_0. There are an infinity of possible approximate solutions, one for each root $Q^{(k)}$. To first order, the solutions can be rewritten as

$$z(y) \approx z^* + 2\left(1-\frac{L}{L_O}\right)^{\frac{1}{2}}\sqrt{M\overline{M}}\cos(y). \tag{36}$$

[2] Symbolic manipulations to obtain (35) were performed using the Maple mathematical software package.

The amplitude coefficient $M\overline{M}$ is positive, which implies that the equation can be solved only for λ_2 of a specific sign, thereby indicating the direction for loss of stability at the bifurcation. The coefficients of the expansions of $a(z)$ and $D(z)$ may be obtained from the fitted analytical expressions for the dispersion and restitution curves. We carry out these computations in the last section.

3.4. Numerical simulation of the IDE. Equation (14) can be integrated using a simple forward method, subject to the constraints imposed by the ring geometry. Initial conditions must be specified by giving the value of $t_r(x)$ over the interval $[-L, 0)$. The finite-difference equation for t_r is given by

$$t_r^{n+1} = \sum_{i=n-N+1}^{n} \frac{\triangle x}{c(t_r^i)} - a(t_r^{n-N+1}), \tag{37}$$

where the integral is evaluated using a simple trapezoid rule, using $\triangle x = L/N$, $N = 200$. This discretized version of the delay equation is identical to the discrete model of propagation on a ring developed by Ito and Glass [7]. They studied in detail the stability of this discrete finite-difference scheme and obtained results similar (but not identical) to our stability results for the continuous IDE. In the discrete model, the stability criterion for the steady state includes a dependence on the slope of the dispersion relation that is not present in the IDE. Our experience with (37) has also revealed a sensitivity of the solution to discontinuities in the initial conditions, which is partly a property of the IDE (see [6]) and a consequence of our sharp front assumption in constructing it. In spite of the discrepancies between the finite-difference equation and the IDE, we use (37) to simulate the dynamics of (14).

In the numerical simulations of the IDE, the steady state $t_r(x) = t_r^*$ is destabilized as the ring circumference is decreased from $L = 13.5$ cm to $L = 13.45$ cm. Starting with initial conditions corresponding to the approximated value of the steady state, growing oscillations are observed in all measured quantities at $L = 13.15$ cm. Figure 9 shows a trace of $C(x)$, $A(x)$, $t_r(x)$, and $T(x)$ after stabilization of the oscillations. The wavelength of the oscillation is $\Lambda \approx 25.7$ cm. As in the PDE, the dynamics of the various measurements at a fixed location along the ring are quasiperiodic. Figure 10 shows the sequence of recovery times t_r and circulation periods T measured during consecutive turns at a fixed location along the ring. Figures 9 and 10 should be compared with Figs. 3 and 4 obtained from the PDE.

Oscillating solutions with a period slightly less than twice the ring length evolve from near steady-state initial conditions in the IDE when $L \leq 13.45$. We do not observe the kind of bistability between steady-state and oscillating solutions found in the PDE. This feature of the PDE may be related to the splitting of the restitution curves which is not taken into account in the IDE model and reflects a breakdown in our slow manifold assumption for the BR model.

Based on the analysis of the IDE, it might be possible to observe oscillating solutions at one of the other frequencies that are known to become unstable at the bifurcation. For example, the second lowest frequency corresponds to a wavelength Λ_1 slightly less than two thirds the ring length. We have obtained such a solution using initial conditions in the form of a low-amplitude sine wave of the correct frequency (as predicted by (30)) over the initial interval $[0, L)$. Figure 11 shows a plot of $C(x)$, $A(x)$, $t_r(x)$, and $T(x)$, illustrating the solution with wavelength close to $2L/3$ after transients have dissipated. Figure 12 shows the sequence of recovery times t_r and circulation periods T measured during consecutive turns at a fixed location along the ring.

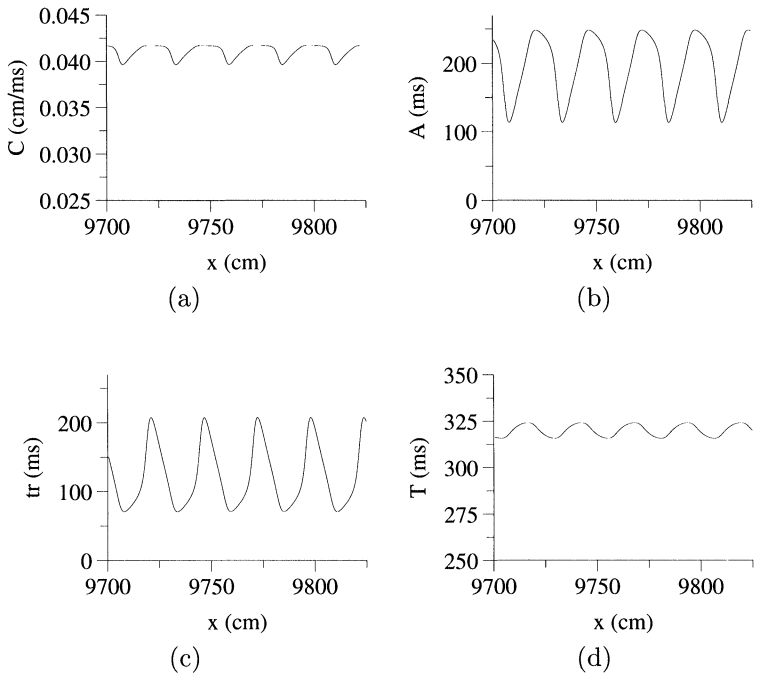

FIG. 9. *Dynamics of a circulating pulse on a ring of length* $L = 13.15$ *cm found from numerical integration of the IDE.* (a) *Speed* $C(x)$, (b) *pulse duration* $A(x)$, (c) *recovery time* $t_r(x)$, (d) *circulation period* $T(x)$. *Transients have dissipated. Wavelength is* $\Lambda = 25.7$ *cm.*

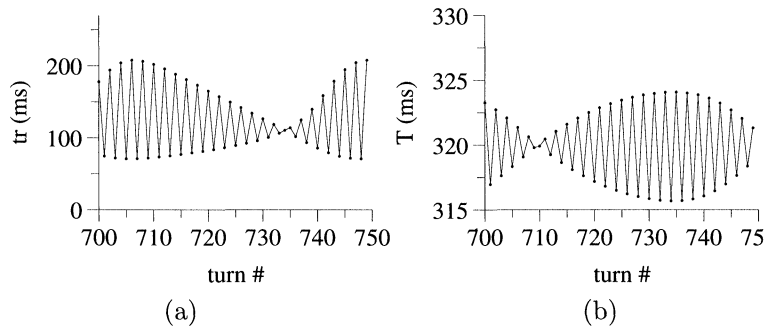

FIG. 10. *Dynamics of a circulating pulse in a ring of length* $L = 13.15$ *cm found from numerical integration of the IDE. Plot of* (a) *the recovery time* t_r *and* (b) *the circulation period* T *as a function of the number of turns around the ring at a fixed location.*

4. The PDE model revisited. Our theory of pulse circulation on a ring is based on a reduction of the dynamics to a simple IDE, using the dispersion and recovery curves to capture the essential features of the nonlinear PDE model. We compare theoretical predictions and numerical results in more detail here.

Numerical simulation of the BR model shows that steady circulation becomes unstable at a ring length $L \approx 13.4$ cm, where the steady-state recovery time is $t_r^* \approx 112$ ms. Numerical integration of the IDE shows loss of stability between $L = 13.5$ cm

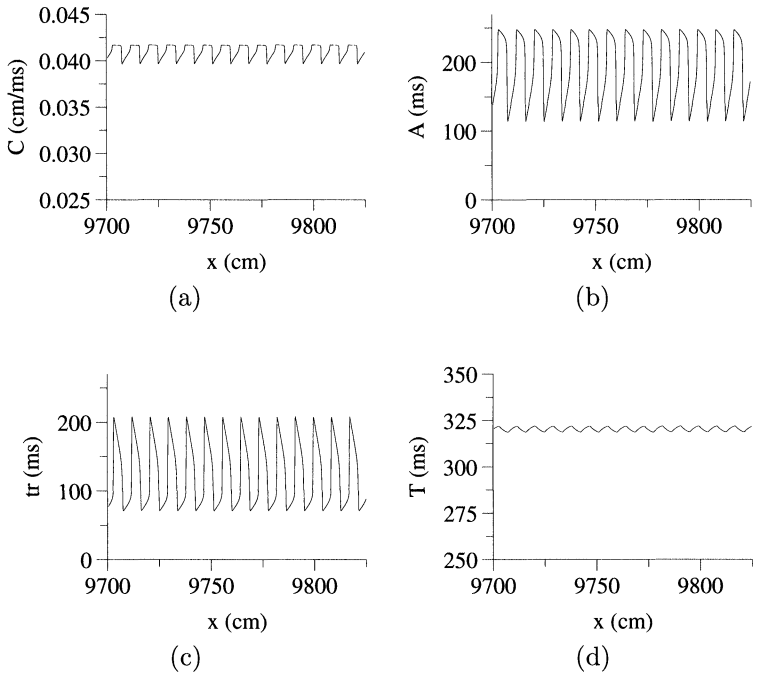

FIG. 11. *Dynamics of a circulating pulse in a ring of length* $L = 13.15$ *cm found from numerical integration of the IDE. Initial conditions were chosen so that an alternate solution of wavelength close to* $2L/3$ *is observed.* (a) *Speed* $C(x)$, (b) *pulse duration* $A(x)$, (c) *recovery time* $t_r(x)$, (d) *circulation period* $T(x)$. *Transients have dissipated. Wavelength is* $\Lambda = 8.74$ *cm.*

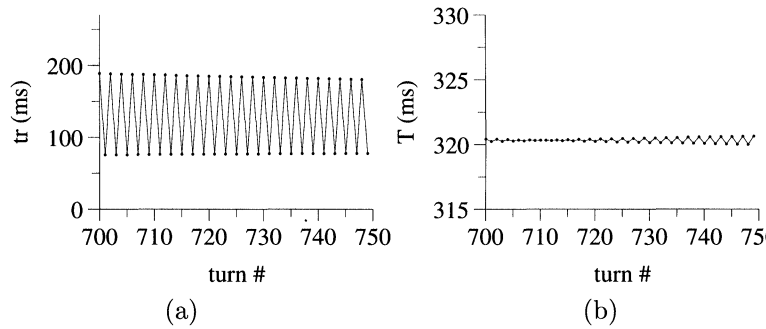

FIG. 12. *Dynamics of a circulating pulse in a ring of length* $L = 13.15$ *cm found from numerical integration of the IDE. Initial conditions were chosen so that an alternate solution of wavelength close to* $2L/3$ *is observed. Plot of* (a) *the recovery time* t_r *and* (b) *the circulation period* T *as a function of the number of turns around the ring at a fixed location.*

and $L = 13.45$ cm. Stability analysis of the IDE predicts a loss of stability when $a'(t_r^*) = 1$. Using the slope of the restitution curve given in Eq.(16), the bifurcation is predicted at $t_r^* \approx 112.6$ ms, corresponding to a ring of length $L_0 = 13.48$ cm.

Nonlinear analysis of the IDE near the bifurcation yields an estimate for the amplitude of the oscillating solutions as a function of the size of the ring. Using our fitted analytical expressions for $a(t_r)$ and $c(t_r)$, we substitute their Taylor expansion coef-

ficients into (35) to obtain the amplitude estimate. Since $M\overline{M}$ is positive, solutions are obtained from (35) only for $\lambda_2 < 0$ (we use $\lambda_2 = -1$, without loss of generality), which is consistent with the direction for loss of stability at the bifurcation. Figure 13 illustrates the predicted maximum and minimum of oscillating solutions near the bifurcation based on (36). Note that we are plotting the prediction for $k = 0$, the lowest-frequency mode. The prediction for subsequent modes would be nearly identical, given that the dependence of $M\overline{M}$ on the mode number, arising as a result of the q_0^2 term in (35), is already saturated at the smallest value of q_0 corresponding to $k = 0$. The value of $\sqrt{M\overline{M}}$ increases only slightly from about 173.7 for $k = 0$ to 174.3 for $k = 1$. Because of the rapid growth in amplitude predicted by theory and the presence of bistability in the PDE simulations, we were able to make a detailed comparison of the amplitude predictions for the IDE simulations only. We have included in Fig. 13 results from numerical simulation of the IDE for the solutions at $k = 0$ (circles) and $k = 1$ (crosses, superimposed on the data points for $k = 0$). There is good agreement between the theory and simulations close to the bifurcation. As expected, the agreement breaks down further from the bifurcation. For $L = 13.15$ cm and $k = 0$, the predicted amplitude is about 108.7 ms. The observed amplitude in the PDE (Fig. 3(c)) is about 163 ms, while in the IDE it is about 137 ms (Fig. 9(c)). Nevertheless, we use the amplitude estimate to obtain an rough approximation for the smallest ring length $L^{\min}$ that will support propagation. Assuming that propagation failure occurs whenever t_r falls below 37 ms and using the first-order solution of (36),

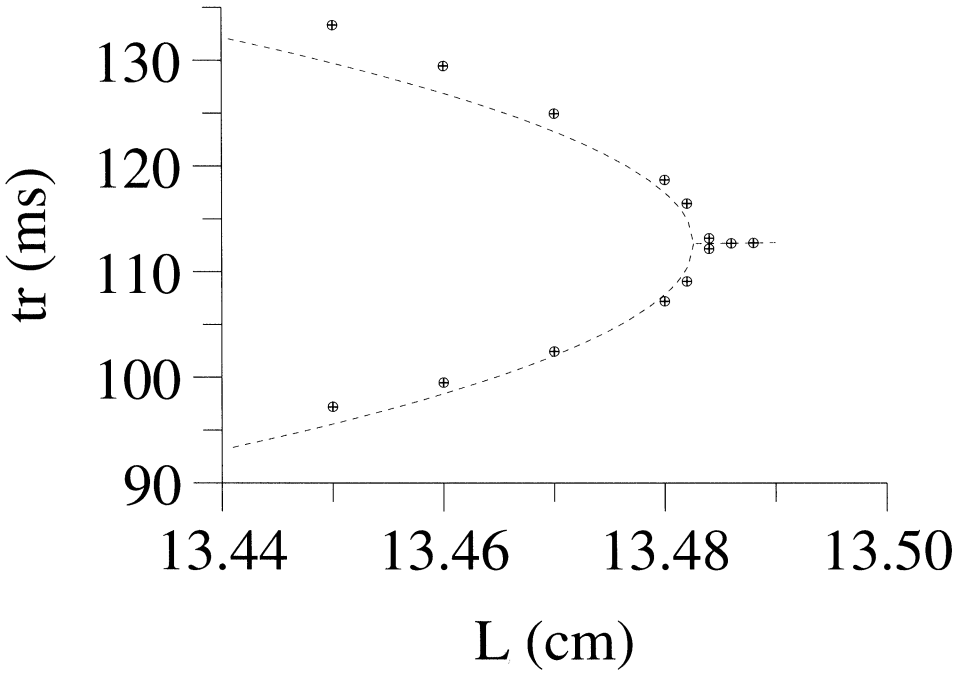

FIG. 13. *Bifurcation diagram for the IDE. The dashed line represents the maximum and minimum value of the periodic solution predicted by* (35) *and* (36) *for the lowest-frequency mode* ($k = 0$). *The predicted values for* $k = 1$ *would differ by only a fraction of a millisecond (slightly larger amplitude). The superimposed data points are from numerical solution of the IDE. The circles correspond to the* $k = 0$ *mode, while the crosses correspond to the* $k = 1$ *mode.*

we find $L^{\min} \approx 12.85$ cm. The PDE simulations reveal that the actual minimum ring length is smaller, between 11 and 12 cm, reflecting the inaccuracy of the first-order solution (36) far from the bifurcation.

Within the range of unsteady circulation, the wavelength of oscillations in the PDE model was slightly less than twice the ring length. Analysis of the IDE shows an infinite-dimensional Hopf bifurcation when $a'(t_r^*) = 1$. We have shown that the growth rate near the bifurcation is lowest for the lowest-frequency mode ($k = 0$ in (29)). Hence, this cannot explain the dominance of this mode as circulation becomes unstable. Our nonlinear analysis near the bifurcation also shows that the amplitude of periodic solutions near the bifurcation increases slightly (but quickly saturates) as the mode frequency increases. Given that the differences in growth rates and amplitude are quite small, higher-order interactions between the modes may contribute to the stabilization of the solution as observed in the numerical simulation. Alternate solutions may also be possible in the PDE, given appropriate initial conditions. The IDE simulations indicate that there are a number of periodic solutions that appear beyond the bifurcation, with frequency close to the frequency of the unstable modes.

We were able to obtain an oscillating solution in the PDE model with wavelength $\sim 2L/3$, corresponding to the predicted mode $\Lambda^{(1)}$ of the IDE. The initial conditions for the PDE model were generated using a stable $2L/3$ solution computed numerically from the IDE at $L = 13.15$ cm. We computed a single action potential using the BR model ($D = 0$ in (1)) and used it to construct a table of the state of the BR medium as a function of the recovery time (negative recovery time falls *during* the action potential). The initial conditions $\mathbf{state}(x)$ can then be read off the table $\mathbf{table}(t)$ using the simple formula

$$\mathbf{state}(x) = \mathbf{table}(t_r(x) - x/C), \tag{38}$$

where C is the wavespeed and assumed to be constant. The initial conditions generated in this way gave rise to the predicted solution. We were able to decrease the size of the ring from $L = 13.15$ cm while maintaining the solution and observing the expected changes in amplitude. Figure 14 shows the evolution of $C(x)$, $A(x)$, $t_r(x)$, and $T(x)$ for the solution at $L = 13.15$ cm after about 250 rotations around the ring. The small variations in peak amplitude visible in the plot of $t_r(x)$ are transient and disappear (variations less than 0.05 ms) within the next 400 rotations. Figure 15 shows the sequence of recovery times t_r and circulation periods T measured during consecutive turns at a fixed location along the ring.

The amplitude of the oscillations in recovery time in Fig. 14 is ~ 146 ms. The amplitude of the numerical solution of the IDE in Fig. 11 is ~ 136 ms. The prediction from (35) is ~ 109.1 ms. The IDE analysis predicts that there should be a very slight increase in the solution amplitude upon moving to higher-frequency solutions (0.4 ms at $L = 13.15$ cm). A slight decrease (less than 1 ms) is observed in the IDE simulations. However, there is a significant decrease in the amplitude of the 2L/3 solution compared to the 2L solution in the PDE. In addition, we were not able to increase the ring size from $L = 13.15$ cm without losing the 2L/3 solution, which slowly drifted towards the 2L solution. Our attempts at obtaining initial conditions for a 2L/3 solution at $L = 13.25$ cm using the method described above also failed. We speculate that the presence of diffusion in the PDE model may be shifting the bifurcation point for the short-wavelength modes to a higher value of a' as well as reducing their amplitude. In other words, there may not be an infinite number of modes becoming unstable *simultaneously* in the PDE, as in the IDE.

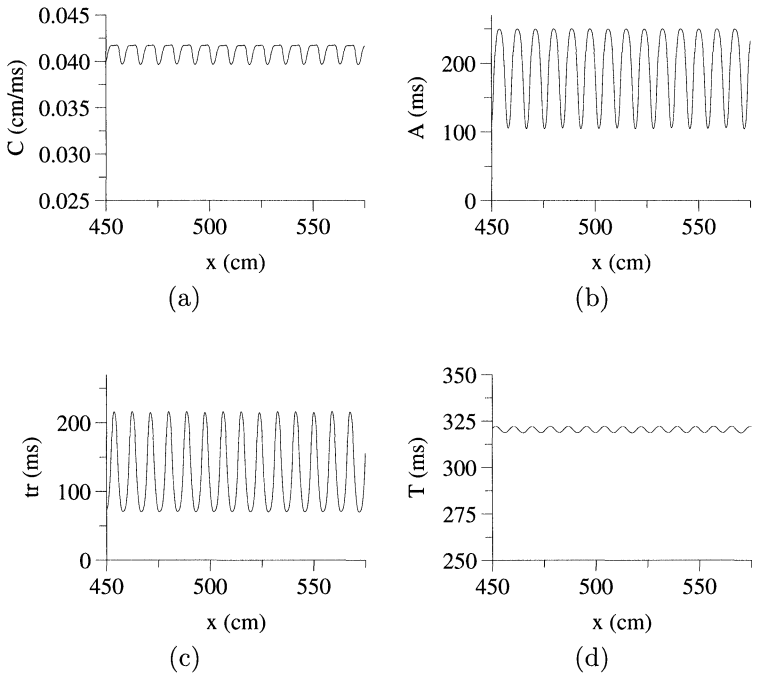

FIG. 14. *Dynamics of a circulating pulse on a ring of length* $L = 13.15$ *cm found from numerical integration of the BR equations. The initial conditions were constructed to obtain an alternate solution at period* $2L/3$. (a) *Speed* $C(x)$, (b) *pulse duration* $A(x)$, (c) *recovery time* $t_r(x)$, (d) *circulation period* $T(x)$. *Transients have dissipated. Wavelength is* $\Lambda = 8.8$ *cm.*

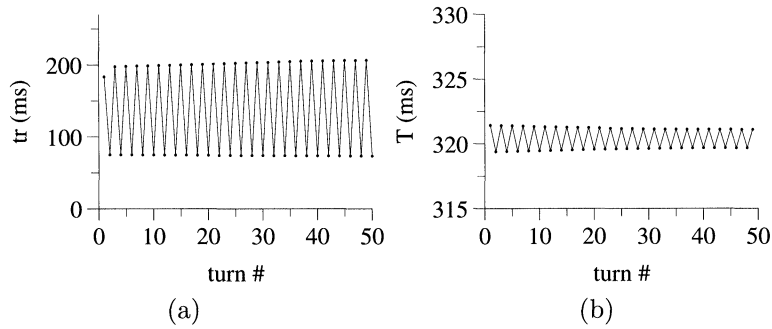

FIG. 15. *Dynamics of a circulating pulse in a ring of length* $L = 13.15$ *cm found from numerical integration of the BR equations. The dynamics are from the alternate solution at period* $2L/3$. *Plot of* (a) *the recovery time* t_r *and* (b) *the circulation period* T *as a function of the number of turns around the ring at a fixed location.*

Estimates for the wavelengths of the two oscillating solutions observed in the PDE and IDE models can be obtained using our eigenvalue expansion near the steady state, assuming that the final solutions are closely related to the original unstable modes. Using (30) at $L = 13.15$ cm, with $\epsilon = 0.148$ and $d' = -0.105$, yields $\Lambda^{(0)} \approx 25.8$ cm and $\Lambda^{(1)} \approx 8.75$ cm. The wavelengths observed in the PDE model are 25.9 cm and

8.8 cm, respectively, while in the IDE numerical simulations they are 25.7 cm and 8.7 cm.

Numerical simulation of the IDE reveals that the equation is sensitive to discontinuities in the initial conditions, as pointed out in [6] for the case of the related neutral differential-delay equation. In addition, the discretized equation that we have used in our integration scheme supports large amplitude oscillations at arbitrarily large frequency [7] for certain choices of restitution and dispersion relations. This is a potential problem in extending the applicability of this theory to other systems. Although the analysis of the IDE remains valid, there may be problems in simulating it numerically. Hence, a better method is needed to compute numerically the periodic solutions of the IDE. In spite of this, we expect that the analytical predictions based on the IDE will be valid in excitable systems where our assumptions about the uniqueness of the restitution and dispersion relations are satisfied. These criteria are directly related to the assumptions made in deriving the IDE directly from the general two-variable system.

In the PDE, it appears that there are nonlinear effects involved in the selection and interaction of the modes beyond what we have described in this analysis, and in fact potentially beyond what can be captured in the IDE. This may be especially true of the relative basins of attraction of the various solutions and how they interact in the PDE model. For example, the infinite-dimensional Hopf bifurcation observed in the IDE probably does not occur in the PDE. As hinted to by our results, the unstable modes do not appear simultaneously in the PDE but arise in turn, with the lowest-frequency mode ($k = 0$) becoming unstable first, followed by higher-frequency modes at shorter ring length. This could be corrected by adding a term to mimic the effect of diffusion in the IDE. In spite of these shortcomings, the IDE formulation presented here not only provides a novel and accurate description of phenomena observed in the PDE model but uncovers uncharted dynamics that may not have been observed otherwise and could prove important in understanding the behavior of excitable media in other contexts.

Appendix. This appendix gives a detailed listing of the BR equations implied by the current term I_{BR} in (1). The total current I_{BR} is the sum of four currents carried by potassium (I_K time-independent outward current, I_x time-activated outward current), sodium (I_{Na} fast inward current), and calcium (I_s slow inward current):

$$I_{BR} = I_K + I_x + I_{Na} + I_s. \tag{39}$$

I_K is given by the time-independent function of voltage,

$$I_K = 4\ 0.35\frac{e^{0.04(V+85)} - 1}{e^{0.08(V+53)} + e^{0.04(V+53)}} + 0.2\ 0.35\frac{V + 23}{1 - e^{-0.04(V+23)}}. \tag{40}$$

The other three currents involve the time-dependent gating variables m, h, j, x, d, and f. We have

$$I_{Na} = (g_{Na}\ m^3\ h\ j + g_{NaC})(V - E_{Na}), \tag{41}$$

$$I_x = 0.8\ x\frac{e^{0.04(V+77)} - 1}{e^{0.04(V+35)}}, \tag{42}$$

$$I_s = g_s\ d\ f(V - E_s), \tag{43}$$

where $g_{Na} = 4$ mS/cm^2, $g_{NaC} = 0.003$ mS/cm^2, $g_s = 0.09$ mS/cm^2, $E_{Na} = -50$ mV, and $E_s = -82.3 - 13.0287 \ln(c)$. The calcium concentration c satisfies

$$\frac{dc}{dt} = -10^{-7} I_s + 0.07(10^{-7} - c). \tag{44}$$

The gating variables all obey equations of the form

$$\frac{dx}{dt} = \frac{x_\infty - x}{\tau_x}, \tag{45}$$

where $x_\infty = \alpha_x/(\alpha_x + \beta_x)$ and $\tau_x = 1/(\alpha_x + \beta_x)$. The form of the equation is the same for all gating variables. The rate constants (α's and β's) depend on voltage and are given by

$$\alpha_x = \frac{0.0005e^{0.083(V+50)}}{1 + e^{0.057(V+50)}}, \quad \beta_x = \frac{0.0013e^{-0.06(V+20)}}{1 + e^{0.04(V+20)}}, \tag{46}$$

$$\alpha_m = \frac{V + 47}{1 - e^{-0.1(V+47)}}, \quad \beta_m = 40e^{-0.056(V+72)}, \tag{47}$$

$$\alpha_h = 0.126e^{-0.25(V+77)}, \quad \beta_h = \frac{1.7}{1 + e^{-0.082(V+22.5)}}, \tag{48}$$

$$\alpha_j = \frac{0.055e^{-0.25(V+78)}}{1 + e^{-0.2(V+78)}}, \quad \beta_j = \frac{0.3}{1 + e^{-0.1(V+32)}}, \tag{49}$$

$$\alpha_d = \frac{0.095e^{-0.01(V-5)}}{1 + e^{-0.072(V-5)}}, \quad \beta_d = \frac{0.07e^{-0.017(V+44)}}{1 + e^{0.05(V+44)}}, \tag{50}$$

$$\alpha_f = \frac{0.012e^{-0.008(V+28)}}{1 + e^{0.15(V+28)}}, \quad \beta_f = \frac{0.0065e^{-0.02(V+30)}}{1 + e^{-0.2(V+30)}}. \tag{51}$$

Acknowledgments. The authors would like to thank A. T. Winfree for helpful comments.

REFERENCES

[1] G. W. Beeler and H. Reuter, *Reconstruction of the action potential of ventricular myocardial fibers*, J. Physiol., 268 (1977), pp. 177–210.

[2] M. Courtemanche and A. T. Winfree, *Re-entrant rotating waves in a Beeler–Reuter based model of two-dimensional cardiac activity*, Internat. J. Bifur. Chaos Appl. Sci. Engrg., 1 (1991), pp. 431–444.

[3] M. Courtemanche, L. Glass, and J. P. Keener, *Instabilities of a propagating pulse in a ring of excitable media*, Phys. Rev. Lett. 70 (1993), pp. 2182–2185.

[4] L. H. Frame and M. B. Simson, *Oscillations of conduction, action potential duration, and refractoriness*, Circulation, 78 (1988), pp. 1277–1287.

[5] M. R. Guevara, G. Ward, A. Shrier, and L. Glass, *Electrical alternans and period-doubling bifurcations*, IEEE Comp. Cardiol., (1984), pp. 167–170.

[6] J. Hale, *Theory of Functional Differential Equations*, Springer-Verlag, New York, 1977.

[7] H. Ito and L. Glass, *Theory of reentrant excitation on a ring*, Phys. D, 56 (1991), pp. 84–106.

[8] H. Ito and L. Glass, *Spiral breakup in a new model of discrete excitable media*, Phys. Rev. Lett., 66 (1991), pp. 671–674.
[9] A. Karma, *Spiral breakup in model equations of action potential propagation in cardiac tissue*, Phys. Rev. Lett. 71 (1993), pp. 1103–1106.
[10] A. Karma, H. Levine, and X. Zou, *Theory of pulse instabilities in electrophysiological models of excitable tissues*, Phys. D, 73 (1994), pp. 113–127.
[11] T. J. Lewis and M. R. Guevara, *Chaotic dynamics in an ionic model of the propagated cardiac action potential*, J. Theor. Biol., 146 (1990), pp. 407–432.
[12] G. R. Mines, *On circulating excitations in heart muscles and their possible relation to tachycardia and fibrillation*, Trans. Roy. Soc. Can., 4 (1914), pp. 43–53.
[13] W. Quan and Y. Rudy, *Unidirectional block and reentry: A model study*, Circ. Res., 66 (1990), pp. 367–382.
[14] J. Rinzel and J. B. Keller, *Traveling wave solutions of a nerve conduction equation*, Biophys. J., 13 (1973), pp. 1313–1337.
[15] A. Vinet, D. R. Chialvo, D. C. Michaels and J. Jalife, *Nonlinear dynamics of rate-dependent activation in models of single cardiac cells*, Circ. Res., 67 (1990), pp. 1510–1524.
[16] A. Vinet and J. L. Leon, *Circulation of activity in a loop of model myocardial cells*, IEEE Eng. Med. Biol. Soc., 13 (1991), pp. 508–509.
[17] A. Vinet and F. A. Roberge, *The dynamics of sustained reentry in a ring model of cardiac tissue*, Ann. Biomed. Eng., 22 (1994), pp. 568–591.
[18] A. T. Winfree, *Electrical instability in cardiac muscle: Phase singularities and rotors*, J. Theor. Biol., 138 (1989), pp. 353–405.
[19] V. S. Zykov, *Simulation of Wave Processes in Excitable Media*, Manchester University Press, Manchester, UK, 1987.